



TECHNICAL ARTICLE

# Effect of Ag Doping on the Microstructure and Electrochemical Response of TiAlN Coatings Deposited by DCMS/HiPIMS Magnetron Sputtering

Wolfgang Tillmann, Diego Grisales, Aida M. Echavarría , Jorge A. Calderón, and Gilberto Bejarano Gaitan

Submitted: 29 July 2021 / Revised: 4 November 2021 / Accepted: 13 November 2021 / Published online: 3 January 2022

**Incorporation of silver particles in nitride coatings has been used to improve the mechanical resistance of steels, but few details are known about the effect of the incorporation of these metals on the electrochemical behavior. In order to evaluate the corrosion resistance and the possible formation of a galvanic couple between the ceramic matrix of TiAlN and the metallic Ag, a TiAlN composite coating doped with four different contents of silver (0.8-25 at.%) was deposited on AISI H11 hot working steel, using the hybrid DCMS/HiPIMS magnetron sputtering technique. The microstructure, topography, elemental chemical, and phase composition of the coatings were determined using SEM/EDS, AFM, XRD, and XPS characterization techniques. The electrochemical behavior was evaluated by electrochemical impedance spectroscopy (EIS) and potentiodynamic polarization. The TiAlN matrix and TiAlN(Ag)-coated samples exhibit higher impedance modulus values than steel substrate, indicating better anticorrosion performance. The anodic current density of the Ag-doped coating increases with the Ag content, suggesting enhanced silver release to the surrounding electrolyte. The TiAlN coating doped with 0.8 at.% silver exhibited the highest corrosion resistance at long immersion times. Finally, it must be noted that all the coatings exhibited corrosion protection to the AISI H11 steel substrate.**

**Keywords** corrosion resistance, DCMS/HiPIMS, electrochemical behavior, silver nanoparticles, TiAlN

## 1. Introduction

In recent decades, efforts to increase the useful life of hot working steels (HWS) such as AISI H11 have gone from plasma nitriding processes through the formation of nitrogen-martensite zones ( $\alpha'$ -Fe (N) content that hardens the surface (Ref 1), to surface modification methods based on nitrides (Ref 2). Although the AISI H11 steel has many advantages such as its high hardness, low deformation during thermal treatments, and excellent resistance to thermal cracking, it has sought to improve the wear resistance of this material since its applications are mainly aimed at tools that work at temperatures from 200 °C to approximately 540 °C (1000 °F) with brief exposures up to 595 °C (1100 °F) (Ref 3). The main applications of this steel are extrusion dies for light alloys, liners for extrusion, tools for die casting, punches and dies for the press, hot cutting

blades, extrusion, and injection molds for polymeric materials, among others. The above uses require not only the dimensional stability of the tools but also a high resistance to wear and to corrosion at high temperatures according to the manufacturing process (Ref 2). Although this steel is selected as the substrate material, it is not normally subjected to environments rich in chlorine ions. The suggested TiAlN matrix coating is indicated to improve resistance to wear, oxidation, and corrosion at high temperatures and even in very aggressive aqueous environments. TiAlN has been used, for example, for coating 304 and 316L stainless steel substrates used in the chemical and biomedical industry enter in contact with Cl-containing corrosive medium which has strong effects in promoting localized corrosion (Ref 4, 5). Other applications of TiAlN coatings, where high corrosion resistance is required, are in the pulp and paper manufacturing industry, in wood-cutting processes, medical applications, mold industry, automotive (especially for brake pads), among others (Ref 6). On the other hand, the manufacture of hard coatings through physical deposition techniques in the vapor phase opens up a range of possibilities, including the use of the multiple advantages of the utilization of hybrid coatings, combining high power impulse (HiPIMS) and direct current (DCMS) magnetron sputtering, which allows the use of different proportions of the voltage used in each one, guaranteeing the high deposition rates provided by DCMS (Ref 7) and the high capacity to improve the ionization of the species during the deposition as a result of an ultra-dense plasma that produces HiPIMS (Ref 8, 9). A comprehensive investigation on the difference of the TiAlN coatings deposited using DC, HiPIMS, and hybrid (DC/HiPIMS) technologies was previously performed by Tillmann et al (Ref 10). The search for better mechanical properties culminates with the development

**Wolfgang Tillmann** and **Diego Grisales**, Institute of Materials Engineering, TU Dortmund University, Leonhard-Euler-Str. 2, 44227 Dortmund, Germany; and **Aida M. Echavarría**, **Jorge A. Calderón**, and **Gilberto Bejarano Gaitan**, Centro de Investigación, Innovación y Desarrollo de Materiales – CIDEMAT, Universidad de Antioquia, Calle 70 N° 52–21, Medellín, Colombia. Contact e-mails: wolfgang.tillmann@tu-dortmund.de, diego.grisales@tu-dortmund.de, aida.echavarría@udea.edu.co, andres.calderon@udea.edu.co, and gilberto.bejarano@udea.edu.co.

of ternary compounds such as TiAlN coating (Ref 11-13). This kind of compound is considered a promising material for the corrosion protection of metallic substrates that perform in high-temperature conditions (Ref 14, 15). Despite the above, it has been demonstrated that the corrosion resistance of TiAlN is conditioned to the existence of structural defects such as pores, cracks, valleys, and low thicknesses, which serve as channels for the mass transport of the corrosive medium toward the substrate interface coating until the substrate is affected (Ref 16, 17). Several studies have shown that the addition of elements such as silver or copper to binary nitrides, where they are normally insoluble, could functionalize the surface with effects such as solid lubrication of the surface. It can significantly improve the wear resistance at elevated temperatures, despite inducing a reduction in the hardness of the composite material (Ref 18-24). For instance, Mejía and collaborators deposited TiAlN coatings doped with silver and copper nanoparticles. They found that Ag and Cu are insoluble in the ceramic matrix forming a nanocomposite. Moreover, the metallic particles exhibited a solid lubrication action and a high bactericidal effect against *E. coli* and *S. aureus* bacteria (Ref 25, 26). However, some researchers indicated that the corrosion behavior of the nitrides doped with Ag is diminished with the increase in the amount of this metal in the coating, due to the acceleration of the Ag reactions with the medium (Ref 16, 17). Additionally, Ag-doped coatings have drawn tremendous attention due to their anti-bacterial character resulting from the segregation of silver onto the surface of the coatings (Ref 27, 28).

Based on the above-described, the idea of developing silver-doped TiAlN hybrid coatings appears to improve their mechanical resistance but also their corrosion and antibacterial resistance. Nevertheless, there are insufficient studies on the corrosion behavior of these composite coatings, much less on the physicochemical and kinetic phenomena that govern their corrosion processes, and the mechanisms that lead to corrosion deterioration of coated steels are not yet completely clear. Although there are multiple investigations on TiAlN, few exist of this material obtained by the hybrid (DC/HiPIMS) system. Greczynski's group has the greatest contributions in these developments, but they have addressed their works to study the ionization energies during the TiAlN manufacturing process and during the formation of AlN wurtzite-type phases, essentially seeking to improve the hardness of those coatings (Ref 29-32). To the best of the author's knowledge, there are no reports in the literature related to the development of TiAlN coatings doped with Ag particles employing hybrid (DC/HiPIMS) technique, and the study of its electrochemical behavior.

In this study, coatings composed of TiAlN with different Ag contents were deposited on AISI H11 hot working tool steel samples using the hybrid DCMS/HiPIMS magnetron sputtering technique. For the developed coatings, the electrochemical behavior was evaluated as a function of the Ag content, and the results correlated with the obtained microstructure. Likewise, the possible corrosion mechanisms were evaluated and discussed through the use and analysis of the respective equivalent circuits derived from the curves resulting from the electrochemical impedance spectroscopy tests.

## 2. Experimental Details

### 2.1 TiAlN(Ag) Nanocomposite Coating Deposition Procedure

TiAlN(Ag) nanocomposite coatings were deposited by hybrid DCMS/HiPIMS magnetron sputtering technique, on disks (40 mm in diameter and 4 mm in thickness) of AISI H11 steel (HWS). The substrate surfaces were metallographically prepared by grinding (diamond disks of 120, 220, 600, and 1200), lapping (largo 9  $\mu\text{m}$ ), and polishing (diamond spray of 6, 3, and 1  $\mu\text{m}$ ) using a machine TEGRAPOL-21 combined with a TEGRAFORCE-5 holder from the company Struers (Denmark). After this preparation, the samples were heat-treated (austenitizing, quenching, and double tempering), to harden the material up to 50 HRC and achieve the desired phases according to Heat Treater's Guide Practices (Ref 33). Subsequently, the samples are polished again to remove any impurities obtained during the heat treatment process as evidenced in previous investigations (Ref 34). The samples were taken and cleaned using ethanol solution before proceeding to the next step.

To begin with the deposition of the coatings, the metallic substrates were placed inside the CC800/Custom fully automated magnetron sputtering device produced by the company CemeCon (Germany). The versatility of the deposition device allows the deposition of the TiAlN-Ag using a convenient target configuration shown in Fig. 1 and the respective parameters indexed in Table 1. As observed, cathode 1 (DC1) was equipped with an elemental Ag target, cathode 2 (DC2) with a Ti-grade1 target, cathodes 3 and 4 with TiAl60 targets (Ti target with 60 aluminum plugs with a diameter of 15 mm along the sputtering track), and finally, cathodes 5 and 6 (HiPIMS1 and 2, respectively) with TiAl48-12 targets (Ti target with 48 aluminum plugs with a diameter of 12 mm along the sputtering track). The size of all the targets is 500  $\times$  88 mm. As observed in Fig. 1, the cathodes are divided in 2 groups (D1-HiPIMS1-DC3 and DC2-HiPIMS2-DC4) at each side of the device, and in those groups, the cathodes are separated 50 mm to each other. The distance between the surface of the target material and the substrate is approximately 170 mm.

Once the substrates and targets are placed in the positions inside the chamber for ionic cleaning, the substrates were

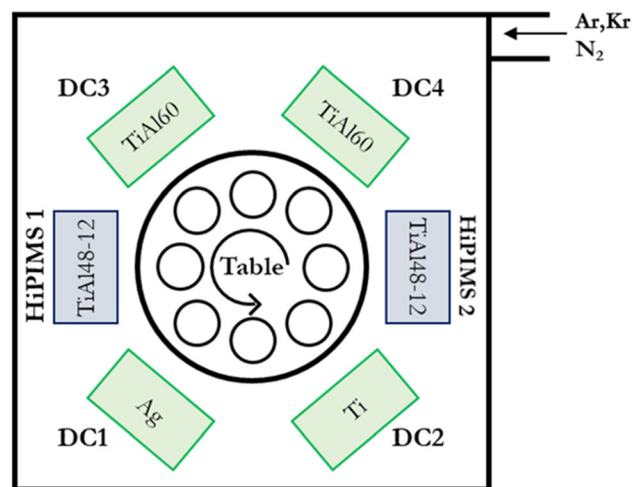


**Fig. 1** Schematic internal configuration of the CemeCon CC800/custom magnetron sputtering reactor

**Table 1 Process parameters of the TiAlN-Ag coatings deposited by hybrid (DCMS/HiPIMS) technique**

Power, W		Gas flow, sccm		Potential, V		Time	
Heating Power during deposition	5000 (~420 °C)	Ar Flow	295	Bias voltage	-80	HiPIMS Pulse duration ( $\mu$ s)	100
DC1	0-1000	Kr Flow	200	Booster	-70	Total deposition time (s)	5720
DC2	2000	N <sub>2</sub> control (mPa)	580				
DC3 and DC4	9500						
HiPIMS 1 and 2							
Average	8000						

exposed to plasma with inert gas etching (Ar flow: 200 sccm, Kr flow: 50 sccm, heating power: 8000 W, temperature: 435 °C, bias: 650 V/ 240 Hz/1600 ns, time: 900 s), booster (metal ion or cathode discharge etching, Ar flow: 240 sccm, Kr flow: 180 sccm, heating power: 8000 W, DC3 and DC4 20 A, Bias DC: 150 V, and time. 900 s), and HiPIMS etching (Ar flow: 240 sccm, Kr flow: 180 sccm, heating power: 2500 W, HiPIMS1: 3500 W, Frequency: 500 Hz, Bias: 1000 V and Time: 1800 s). The etching process is carried out to remove layers of oxides formed on the substrates surface and additional contamination inside the reactor, a fact that plays a key role in coating adhesion (Ref 10).

In the first stage, an adhesion nanolayer of pure metal Ti was deposited (thickness of 25 nm approximately). This layer reduces the residual stress and improves the adhesion in the interface substrate coating (Ref 35-37). The adhesion layer Ti was deposited during 160 s, with an atmosphere of Ar (295 sccm) and Kr (200 sccm) with a power applied to the Ti target of 4000 W and a bias voltage of -100 V. Nitrogen was then added to the Ar and Kr mixture as a pressure control gas until a working pressure of 580 mPa was reached. In the second stage, the TiAlN reference coating and the TiAlN(Ag) nanocomposite coatings were deposited using the parameters depicted in Table 1. In addition to the Ar and Kr flows, the pressure in the deposition chamber was maintained at 580 mPa using the nitrogen flow (approximately 100 sccm). The power applied to the target of Ag was varied in values of 1000 W, 750 W, 500 W, and 250 W to obtain different contents of this metal into the TiAlN nitride. HiPIMS discharges had an average cathode power of 8000 W, a frequency of 1000 Hz, a pulse duration of 100  $\mu$ s. The bias voltage was operated on DC mode at -80 V. The deposition processes of the TiAN-Ag layer lasted 5167 s at a process temperature of approximately 420 °C.

## 2.2 Coatings Characterization

Microstructural analysis of the coatings was carried out through the study of the brittle cross section, and the topography of the TiAlN and TiAlN(Ag) coatings was evaluated using a field emission scanning electron microscope (SEM) JSM-7001F device fabricated JEOL (Japan). Besides, the incorporation of an x-ray detector from Oxford Instruments (UK) into the SEM allows the determination of the chemical composition of the coatings using energy-dispersive x-ray spectroscopy (EDX). An x-ray diffractometer Advance D8 from the company Bruker (Germany) using Cu-K $\alpha$  radiation ( $\lambda=1.5418$  Å, 30 kV, 28 mA) was used to generate phase diffractograms. The  $\theta-2\theta$  mode was used, the scan range from 20 to 150° at steps of 0.05°. To complement the structural

analysis, the XPS assays were performed in ultra-high vacuum (UHV,  $5 \times 10^{-9}$  mbar) on a Specs X-ray photoelectronic spectrometer (NAP-XPS) with a PHOIBOS 150 1D-DLD analyzer, using a monochromatic source of Al-K $\alpha$  (1486.7 eV, 13 kV, 100 W). The spectrometer was calibrated against the Ag3d5/2 (368.53 eV) photoelectron line positions obtained from cleaned silver metallic surfaces. Survey scans were acquired at the pass energy of the analyzer equal to 100 eV, while high-resolution spectra were acquired at 50 eV pass energy with an energy resolution of 0.1 eV. Likewise, 20 measurement cycles for the high-resolution spectra and 3 for the general spectra were performed. The general spectra were measured before and after cleaning the surface with an Ar-ion gun at 3000 V for 1800 s in an area of 1 mm<sup>2</sup>. The high-resolution spectra were measured on the surface after cleaning. The “CasaXPS” software was used to adjust the quantitative peak in narrow spectra of the Ti 2p, Al 2p, Ag 3d, N 1s, and O 1s regions. For the determination of the respective binding energies of the elements of the coating, a correction of the position of the peaks was carried out using as reference the C-C bond in peak C 1s at a binding energy of 284.6 eV. To estimate the roughness value and grain size of the coatings, an Atomic Force Microscope (AFM) MFP-3D-Infinity manufactured by Oxford Instruments (UK) was used. The scanner area corresponded to 5  $\mu$ m<sup>2</sup> with a silicon Al-coated tip AC240TS (radius = 9 nm, a nominal spring contact of 2 N/m, and a resonance frequency of 73.52 Hz) in the AC mode.

## 2.3 Electrochemical Corrosion Testing

The corrosion tests were carried out by electrochemical impedance spectroscopy (EIS) and potentiodynamic polarization (PP) techniques. EIS and PP tests were performed using an Autolab AUT84636 galvanostat-potentiostat system (The Netherlands) with NOVA 1.10 analysis software. All tests were performed in triplicate to ensure the repeatability of results. Coated samples were immersed in 3.5 wt.% NaCl solution at  $25 \pm 1$ °C. These tests were performed in a conventional three-electrode cell, using the coated samples as working electrodes (1.33 cm<sup>2</sup> tested area), a high-purity graphite bar as a counter electrode, and an Ag/AgCl electrode as reference. EIS measurements were performed after 1 hour of immersion (stabilization time) at open-circuit potential (OCP). EIS tests were carried out with a perturbation amplitude of 10 mV, in frequencies between 1 MHz and 5 mHz at room temperature and nine times of exposure (1, 4, 8, 24, 48, 96, 192, 188, and 360 hours). After 360 hrs. of immersion, a potentiodynamic polarization test was conducted in a potential range of -00 to 400 mV versus OCP and a scan rate of 170  $\mu$ V/s. Gamry Echem Analyst software (USA) was used to fit the

impedance curves and to model the representative electrical circuit corresponding to different coatings. The electric circuit elements found during the fitting are the following:  $R_s$  (electrolyte resistance),  $Q_{\text{coat}}$  (coating constant phase element),  $R_{\text{coat}}$  (coating resistance),  $Q_{\text{dl}}$  (double layer constant phase element),  $R_{\text{ct}}$  (charge transfer resistance),  $Q_{\text{oxide layer}}$  (oxide layer constant phase element),  $R_{\text{oxide layer}}$  (oxide layer resistance) and  $W$  (porous-bounded Warburg diffusion element).

### 3. Results and Discussion

#### 3.1 Microstructural Analysis of Coatings

Some basic properties of the hereby developed TiAlN and TiAlN(Ag) coatings are summarized in Table 2. It is important to note that the content of silver increases when the power applied to DC1 target (Ag) increases; although the differences are in the range of powers for these coatings, the atomic percentage of Ag maintains a linear relationship except for the passage from 750 W to 1000 W. This may be due to the supersaturation that undergoes within the matrix, in which the excess of Ag atoms cannot be accommodated in the TiAlN structure with the same efficiency as it occurs at lower powers values. On the other hand, probably, a re-sputtering of accumulated silver on the surface takes place, due to the bias voltage and the high kinetic energy of the adatoms that reach the substrate. Elsewhere, the ratio Ti:Al is almost 1:1, suggesting the fcc (face-centered cubic) phase formation (as shown later in this paper in the XRD analysis), which normally presents high mechanical properties and high wear resistance as reported by other authors (Ref 38).

Figure 2 shows the cross-sectional SEM images, as well as the surface images by SEM and AFM of the TiAlN and TiAlN(Ag), deposited coatings. Even though the deposition time for all the coatings was the same, an increase in their thickness along with the increase in the power applied to the Ag target is observed, due to the increase in the sputtering and deposition rate of silver (Ref 21). All the coatings exhibited a dense columnar structure growth indicating the positive effect of the high energetic HiPIMS deposition mode used in this work, which conduces to a denser microstructure with very low roughness (less to 100 nm) (Ref 39, 40).

Considering that silver is insoluble in most metal nitrides, it is mainly housed between the columnar spaces of the TiAlN

matrix, which probably leads to greater densification of the composite coatings, occupying a great portion of the pores and space between columns of the TiAlN coating. Considering the temperature of 420 °C of the coating deposition process, it is expected that the silver particles lodged between the columnar spaces of the TiAlN matrix will slowly diffuse to the surface of the coating during the deposition time of the composite coating, in such a way that larger particles are formed by agglomeration of silver, also leading to the formation of some Ag clusters. As a result, an increase in the surface roughness of the coating and a cauliflower-like topographic appearance is observed. Although the size of the silver particles on the surface of the coatings was not determined, the SEM images in Fig. 2 suggest a size less than 100 nm. On the other hand, the residual stresses of the coatings, several studies agree that these are reduced by doping the matrix with ductile elements such as silver or copper; this is because incorporating these metals they absorb the energy by deforming elastically and/or plastically when the coating is subjected to an external load (Ref 41-43). In addition, when the silver content increases into the coatings, it is observed the formation of a structure with a large number of interfaces (see Fig. 2c, d, and e). This is the result of the satellite movement of the sample holder and the rotation of the samples, each time they pass in front of the respective targets. A finer grain microstructure, reduction in lattice defects, and formation of interfaces could bring advantages on the corrosion resistance of the coatings due to an increase in the degree of difficulty for the entry of chemical agents until the steel substrate and preventing its corrosion (Ref 36, 44, 45). Moreover, it can be seen in the topographical images of SEM and AFM that the roughness increases with the silver content, giving the appearance of an uneven cauliflower-like structure. Also, the minimization of nanometric structural defects, cracks, and the decrease in grain size improve the protection of the metal substrate against corrosion by decreasing the number of direct electrolyte input channels to the substrate (Ref 46).

Figure 2(f)-(j) shows SEM topographical microstructures of the coatings, while Fig. 2(k)-(o) corresponds to the AFM images of these. The results disclosed the formation of dense and soft structure in the TiAlN matrix coating (Fig. 2f) with equiaxial grains formation, with uniform sizes and with the presence of smaller ones located between the largest. These results are in agreement with the roughness values obtained for this material. It is interesting to note that for Ag contents of 0.8 at.% in the coating, the structure is refined, according to the

**Table 2 Coating's properties: chemical composition, thickness, and roughness of coatings developed**

Sample	Chemical composition, at.%					Ag-target power (W)	Thickness, $\mu\text{m}$	Roughness, nm
	Ti	Al	Ag	N	O			
TiAlN	48.05 $\pm$ 0.08	51.95 $\pm$ 0.08	...	...	...	0	3.10 $\pm$ 0.05	7.2 $\pm$ 0.5
	23.84 $\pm$ 0.35	25.00 $\pm$ 0.41	...	51.17 $\pm$ 0.75	No detected			
TiAlN(Ag)-0.8 at.%	48.98 $\pm$ 0.15	50.22 $\pm$ 0.20	0.79 $\pm$ 0.08	...	...	250	3.20 $\pm$ 0.07	8.5 $\pm$ 0.2
	22.70 $\pm$ 0.27	22.45 $\pm$ 0.34	0.35 $\pm$ 0.03	54.49 $\pm$ 0.67	No detected			
TiAlN(Ag)-10 at.%	43.86 $\pm$ 0.17	46.02 $\pm$ 0.12	10.11 $\pm$ 0.06	...	...	500	3.60 $\pm$ 0.05	18.1 $\pm$ 0.6
	16.12 $\pm$ 0.29	16.21 $\pm$ 0.23	3.68 $\pm$ 0.04	63.63 $\pm$ 0.32	0.36 $\pm$ 0.70			
TiAlN(Ag)-20 at.%	39.44 $\pm$ 0.13	40.91 $\pm$ 0.17	19.65 $\pm$ 0.08	...	...	750	4.20 $\pm$ 0.09	22.0 $\pm$ 1.2
	12.73 $\pm$ 0.04	12.61 $\pm$ 0.11	6.44 $\pm$ 0.05	68.13 $\pm$ 0.53	0.10 $\pm$ 0.41			
TiAlN(Ag)-25 at.%	36.9 $\pm$ 0.08	37.87 $\pm$ 0.21	25.23 $\pm$ 0.20	...	...	1000	4.80 $\pm$ 0.07	68.9 $\pm$ 4.8
	11.12 $\pm$ 0.1	10.88 $\pm$ 0.13	7.82 $\pm$ 0.10	70.02 $\pm$ 0.67	0.17 $\pm$ 0.85			

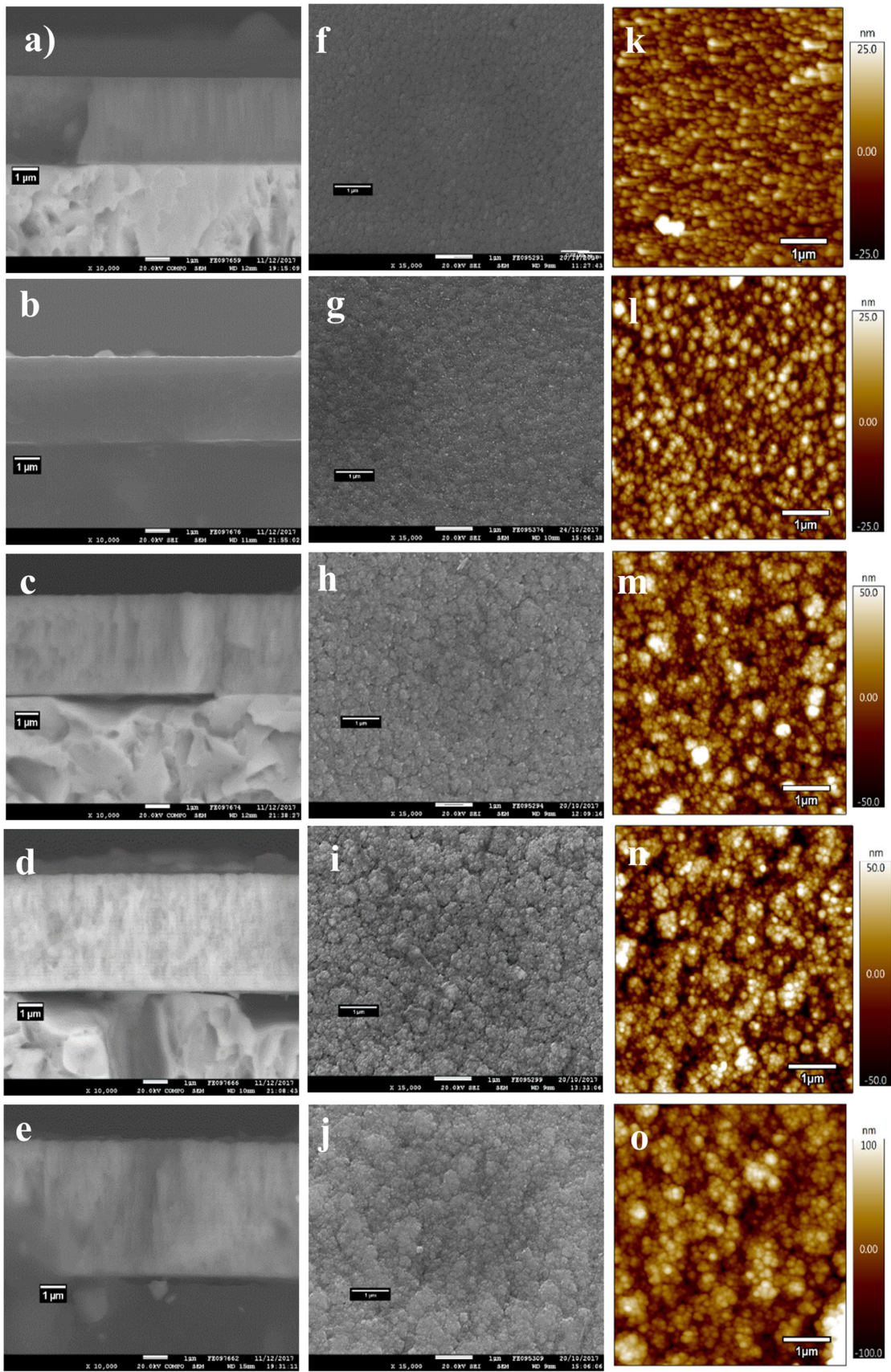


**Fig. 2** (a-e) SEM cross-sectional image—BSE mode, (f-j) SEM topography, and (k-o) AFM image of TiAlN coatings with different contents of Ag. (a) TiAlN, (b) 0.8 at.% Ag, (c) 10 at.% Ag, (d) 20 at.% Ag, and (e) 25 at.% Ag, increasing Ag content from left to right

theory of grain refinement by the inclusion of a low quantity of the immiscible solute in the solid solution (Ag), which stops grain growth due to its precipitation on the grain boundaries. However, for large amounts of silver, an increase in grain size is expected, as suggested by the surface images from AFM (Fig. 2).

This coating shows several small white particles located in grain boundaries, indicating the presence of Ag homogeneously distributed on the surface of the coating. For Ag contents above 10 at.% (Fig. 2h-j and m-o), an irregular granular growth on the surface in the form of cauliflower is observed due to the increased accumulation of Ag near the surface accompanied with greater surface roughness (Ref 47). Mulligan et al. deposited CrN doped with Ag onto stainless steel samples by DC magnetron sputtering, finding that silver contents greater than 12 at.% conduce to a network of under dense pores that form during deposition due to Ag segregation into nm-size pockets and these pores grow in width and connectivity resulting in a more porous structure and rougher surface (Ref 48). Similar results have been reported by De los Arcos et. al, in a TiN matrix doped with Ag. In their investigation, TiN with Ag contents lower than 2 at.% showed high densification and compactness, while Ag contents greater than 15 at.% promoted structures of separate columns, porous and with the presence of small cracks (Ref 49). However, and contrary to Mulligan and De los Arcos, during the current investigation, no porosity is observed in coatings at high Ag content. This result is presumable due to the high bias voltage applied to the substrate (−100 V). High bias voltage also contributes to densifying the microstructure of deposited coatings as it was also observed by De los Arcos et al., who deposited TiN-Ag at different bias voltages (Ref 49). The big size of the Ag clusters formed on the surface of the coatings at high Ag contents diffculted the determination of the grain size. Therefore, it is suggested from topographical SEM and AFM observations in this work that the grain size of the coatings slowly increases with their Ag content.

Figure 3 shows the diffraction patterns of the TiAlN matrix and the four doped coatings with different silver contents. The TiAlN coating exhibits preferential growth in direction (111) corresponding to a cubic fcc structure type NaCl (ICDD PDF# 04-005-5251) and as reported in various works (Ref 50, 51). However, it also exhibits small wide- and low-intensity peaks for directions (200), (220), (311), and (222). Besides, Fe (110), (200), and (211) are visible in the XRD spectrum (Ref 51). The incorporation of 0.8 at% Ag leads to an increase in the intensity of the peak (111) probably due to an increase in its crystallinity generated by the reduction in grain size caused by the silver nanoparticles housed between the columnar spaces of the microstructure of TiAlN, which hinder the growth of the grain in the XY plane, as observed by other authors (Ref 21, 48, 52), and in Fig. 2(f) and (k).

The preferential growth direction (111) of TiAlN coatings was observed by other authors using the magnetron sputtering deposition technique (Ref 50, 51). An explanation for this behavior is given by Gall et al., who calculated the binding and diffusion energies of adatoms, molecules, and small clusters on TiN (001) and TiN (111) surfaces using the density functional methods (Ref 53). In the initial phase of deposition of the coating carried out at a low temperature and far from thermodynamic equilibrium, it is governed by kinetic effects and grows preferentially in the plane (200) of higher atomic density and lower surface energy. However, as the coating

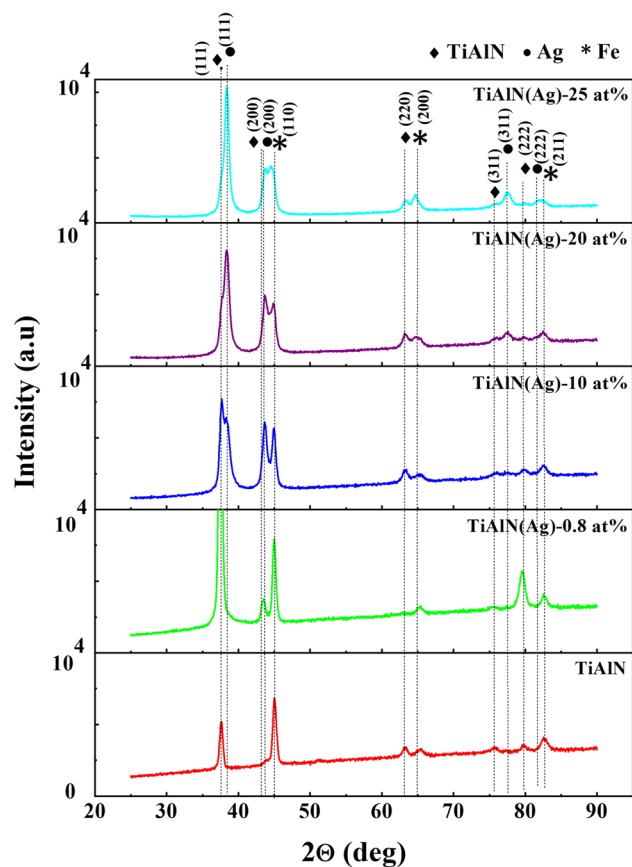
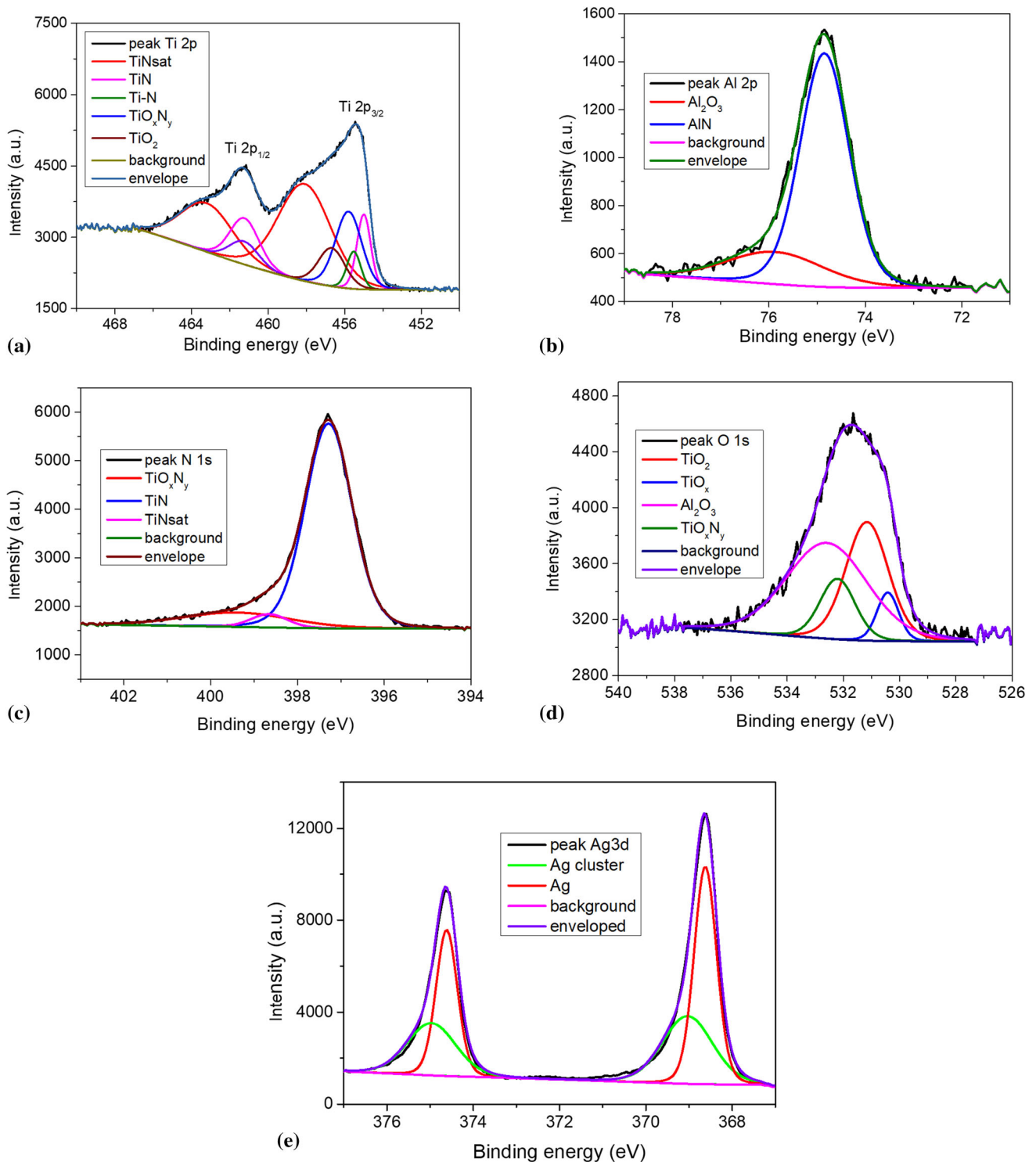


Fig. 3 X-ray diffraction patterns for TiAlN matrix and TiAlN(Ag) coatings

grows, the low mobility of the adatoms leads to a longer residence time and greater incorporation of titanium ions in the plane (111) than in the plane (200) and continues to grow preferentially in the crystallographic direction (111). Additionally, independent peaks of Ag are also observed, which exhibited an fcc structure and grow in the directions (111), (200), (311), and (222) (ICDD card no. 00-004-0783) and increase their intensity with the increase in the silver content in the composite coating, suggesting the insolubility of this metal in the TiAlN ceramic matrix. In the coating with 10 at.% Ag, a shoulder can be seen in the peak (111) of the TiAlN corresponding to silver, indicating a preferential growth of silver in this plane of higher density and lower surface energy, and which later overlap for greater silver contents. However, the Ag (200) peak is also observed since the deposition temperature of 420 °C is sufficient to cause a greater mobility and superficial diffusion of silver to also grow in this plane of higher surface energy. Finally, it is important to notice that Ag (311) and (222) are only evidenced at Ag contents higher than 20 at.%.

Figure 4 shows the deconvoluted high-resolution spectra of Ti 2p, Al 2p, Ag 3d, N 1s, and O 1s of the XPS survey spectra of sample TiAlN (Ag) with silver content equal to 19.6 at.%, whose binding energies were corrected using as reference the C-C bond in peak C 1s at a binding energy of 284.6 eV. The peak Ti 2p presents a doublet in Ti 2p<sub>3/2</sub> and Ti 2p<sub>1/2</sub>, which are separated by 5.9 eV. Ti 2p<sub>3/2</sub> exhibited four peaks for bonds of Ti-N in TiAlN, Ti-N in TiN phase, TiN<sub>x</sub>O<sub>y</sub>, and TiO<sub>2</sub> phases with binding energies of 455.0 eV, 455.5 eV, 455.8 eV, and



**Fig. 4** High-resolution XPS data of TiAlN(Ag)-20 at.% core level spectra of (a) Ti 2p, (b) Al 2p, (c) N 1s, (d) O 1s, and (e) Ag 3d

456.7 eV, respectively, as shown in Fig. 4(a). It should be noted that the Ti-N bond in the TiN detected here was not observed in the XRD due, on the one hand, to its low content in the coating and to the fact that the TiN (111) and TiAlN (111) peaks overlap. Furthermore, a satellite peak of the Ti-N in the TiAlN bond is observed at 458.1 eV. These results agree well with those reported by other authors (Ref 29, 54, 55). In Fig. 4(b) is shown the Al 2p region; in there two peaks are observed: the first one with a binding energy of 74.8 eV is assigned to the Al-

N bond in the TiAlN compound and the second one, at a greater binding energy of 75.8 eV, corresponds to the Al<sub>2</sub>O<sub>3</sub>. Greczynski (Ref 26) reported Al-N binding energy in the high-resolution Al 2p peak between 74.2 and 74.3 eV for the TiAlN coating, values very close to the one found here of 74.8 eV. However, this value may undergo a shift as a function of the aluminum content in the TiAlN and some deposition parameters such as the bias voltage. Considering that no diffraction peaks of the AlN phase were observed in the XRD results, it is

suggested that this bond is from Al-N in TiAlN. It should be noted that a low amount of oxygen was observed in the coatings (by EDS measurements) due to traces of oxygen in the targets and residual oxygen in the vacuum chamber. Further, the prolonged contact of the coated samples with the environment during the other characterization procedures, for example XPS measurements, also led to contamination of their surface with oxygen, which partially reacted with titanium and aluminum formed alumina and titanium dioxide on the coatings surface, which was not completely removed by ion beam-cleaning in the XPS.

The main peak position of 397.2 eV in the N 1s region corresponds to the Ti-N bond in the TiAlN, as shown in Fig. 4(c). The other contribution of the N 1s core level, centered at 399.4 eV, is assigned to N-Ti bonding in the oxide  $TiN_xO_y$  (Ref 30, 54, 55). In addition, a satellite peak is observed at 398.6 eV corresponding to the Ti-N bond in the TiN phase. The deconvolution of the high-resolution O 1s peak shown in Fig. 4(d) exhibits four centered peaks at 530.4 eV, 531.2 eV, 532.2 eV, and 532.6 eV assigned to the oxides of  $TiO_x$  from TiN,  $TiO_2$  from TiAlN,  $TiO_xN_y$ , and  $Al_2O_3$ , respectively. Since these phases were not observed in the XRD analysis of the coatings and their content in the coating is minimal, it is suggested that most of these oxide compounds were formed by atmospheric contamination and they were not completely removed from the surface during the ion beam cleaning in the XPS chamber.

The chemical state of Ag in the evaluated sample TiAlN(Ag)-19.6 at.% silver was analyzed by examining Ag-3d levels as shown in Fig. 4(e). Silver presents a doublet in the 3d orbital exhibiting two peaks for metallic silver Ag-Ag bonds centered at 368.6 eV ( $3d_{5/2}$ ) and 374.6 eV ( $3d_{3/2}$ ) attributed to silver nanoparticles housed in the TiAlN matrix. Two other peaks observed at binding energies of 369 eV and 375 eV are assigned to Ag- clusters formed mainly by agglomeration of silver nanoparticles on the surface of the coating results that are very consistent with those found by Almeida Alves et al.(Ref 56).

The results discussed above demonstrate the existence of TiAlN and Ag phases in the deposited composite coatings, accompanied by a little amount of alumina, titanium dioxide, which probably formed on the surface of the coating due to atmospheric contamination. Table 3 shows the phases identification and the quantitative percentage of Ti 2p, Al 2p, and N 1s.

Al-N and Ti-N bonds are attributed to the TiAlN phase, as discussed above. It is observed that the highest percentage corresponds to the TiAlN phase, evidencing the quality of the coating deposited in agreement with the XRD results. According to XPS results, the percentage contents of the silver nanoparticles and the silver clusters were estimated as 57.23%

**Table 3 Phases identification and the quantitative percentage of Ti 2p, Al 2p, and N 1s**

Ti 2p, at. %				Al 2p, at. %		N 1s, at. %	
TiAlN	TiO <sub>x</sub> N <sub>y</sub>	TiO <sub>2</sub>	TiN	Al-N	Al <sub>2</sub> O <sub>3</sub>	Ti-N	TiO <sub>x</sub> N <sub>y</sub>
73.65	18.06	5.49	2.81	78.58	21.42	86.71	13.29

and 42.77%, respectively. The content of the nanoparticles prevails as expected.

### 3.2 Electrochemical Behavior

#### 3.2.1 Electrochemical Impedance Spectroscopy

(EIS). Figure 5 shows the evolution of the impedance modulus reads at the lowest frequency (5 mHz) at different immersion times of the coatings and the steel substrate samples. A drastic drop in the impedance module for the AISI H11 and the TiAlN was observed during the first ~100 hours of the immersion test. After that, a slight stabilization of the impedance module is attained, with values close to 800 and 10000  $\Omega\text{ cm}^2$  for AISI H11 and the TiAlN samples, respectively. In Ag-doped samples, attenuation of the impedance modulus drop was observed. The decrease in the impedance modulus during the exposure time is due to the interaction of the electrolyte with the surface of the samples and its possible penetration into the structure of the coatings. A slight increase in the value of the impedance module of the substrate sample occurs around 200 hours, which could be related to the passivation of the steel surface by the interaction with the test electrolyte. The TiAlN matrix and TiAlN(Ag)-coated samples exhibited higher impedance modulus values than the steel substrate, indicating that they possess a lower electrochemical activity than the substrate, and consequently, better anti-corrosion performance could be expected from the coated samples.

Although coatings showed higher impedance modules than the AISI H11 substrate, a comparison between coated samples shows that the increase in the amount of Ag into the coating decreases the impedance modulus somewhat, except for the TiAlN(Ag)-0.8at% coating. This sample exhibits the highest impedance modulus after the first 10 hrs of the exposure until the end of the test. This result is related to the less electrochemical activity of this sample due to the large degree of densification of the coatings achieved from the hybrid DCMS/HiPIMS magnetron sputtering technique. The densification of the coating structure was evidenced in the SEM images and the high crystallization level of this coating in the XRD analysis. This is in agreement with results obtained for this type of material reported in previous work, where greater densification of the TaN-Ag coating was also evidenced with the increase in the bias voltage applied to the substrate (Ref 17).

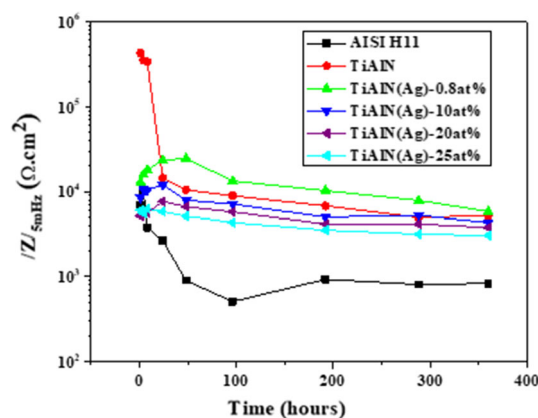


**Fig. 5** Impedance modulus vs. time of immersion in NaCl 3.5wt.% solution for the AISI H11 steel substrate, TiAlN, and TiAlN(Ag) coatings



In the TiAlN(Ag)-0.8%at coating, the small amount of Ag present into the coating fills the micro spaces generated between the columnar grain limits of the TiAlN layer, blocking the entrance of the electrolyte to the material, as could be observed in the superficial structure of Fig. 2(b). The decrease in the impedance modulus of Ag-doped coatings with amounts of Ag equal to and greater than 10 at.% occurs by the dissolution of Ag into the corrosive medium, a phenomenon that has been explained in previous works (Ref 17, 57).

Figure 6 shows the EIS measurements (Nyquist plots) for the TiAlN(Ag) coatings, the AISI H11 steel substrate, and the TiAlN matrix coating; after 1, 192, and 360 hours of exposure in NaCl 3.5 wt.% electrolyte. In Fig. 6(a), it is possible to

observe that during the first hour of the test, all samples, including the steel substrate, show the formation of an open capacitive loop that occupies the entire frequency range. As the formation of this loop starts at high frequencies, this behavior is possibly associated with the charge transfer resistance ( $R_{ct}$ ) in parallel combination with the capacitance of the double electrical layer on the substrate and on the surface of the coatings, during the first hours of immersion. The capacitive loop formed by the H11 steel substrate, during the first hours of the test, tends to close at the limit of zero frequency in the real axis of the impedance, indicating a drop in its resistance upon contact with the electrolyte. On the other hand, the TiAlN matrix coating has the highest value  $Z'$  real ( $2.5 \times 10^5 \Omega \cdot \text{cm}^2$ ),

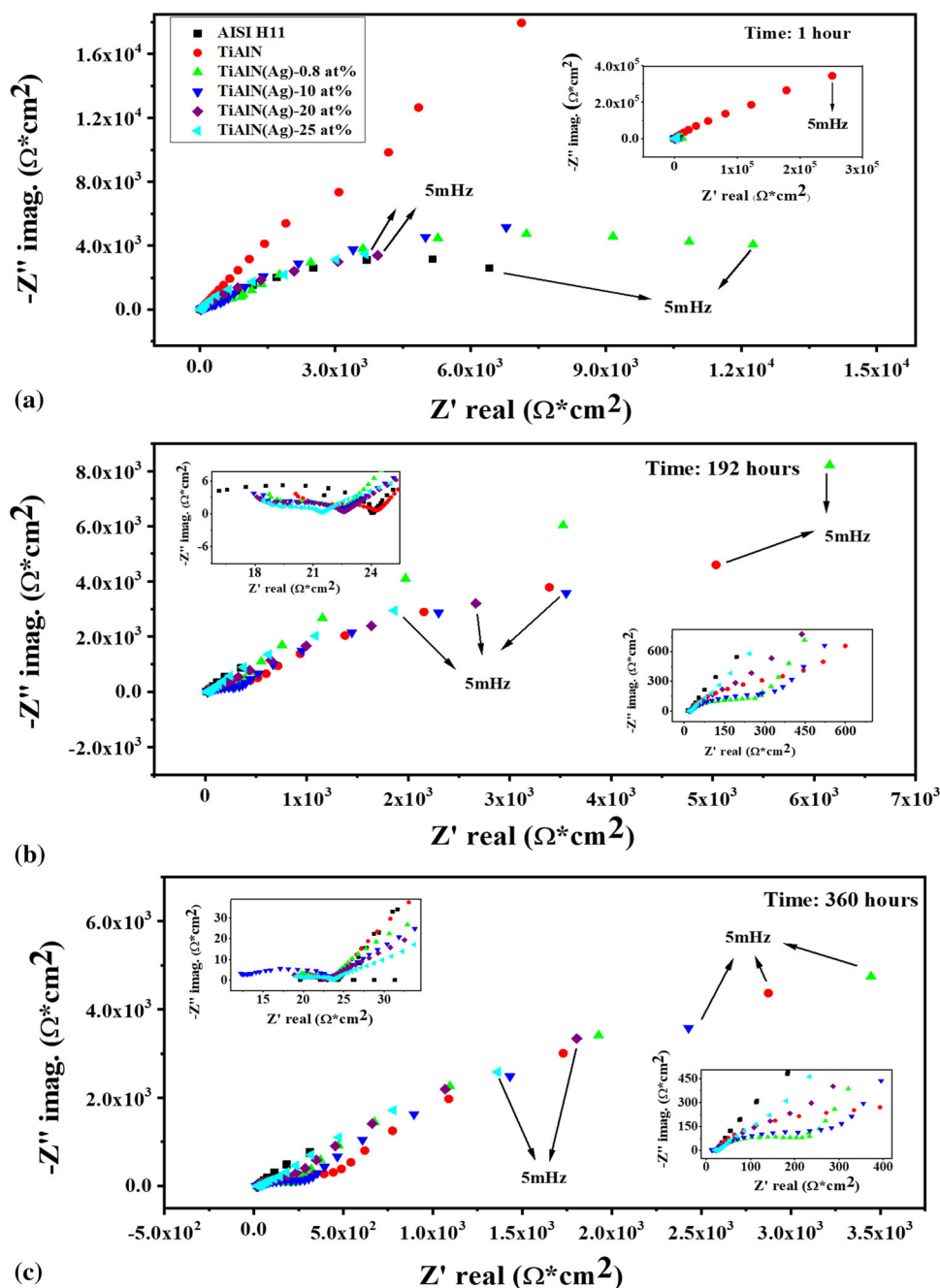


**Fig. 6** Nyquist plots of the electrochemical impedance for the TiAlN(Ag) coatings, the AISI H11 steel substrate, and the TiAlN matrix coating in NaCl 3.5 wt.% electrolyte, at different exposure times, (a) 1 hour, (b) 192hours, and (c) 360 hours

two orders of magnitude higher than other samples, possibly due to the ceramic character of the coating that blocks the entry of the electrolyte during the first immersion times. For Ag-doped coatings, the resistance is lower than the TiAlN matrix, and moves in an interval of  $0.35 \times 10^3 \Omega \text{ cm}^2$ – $1.2 \times 10^4 \Omega \text{ cm}^2$ , indicating a higher electrochemical activity with the incorporation of Ag into the coatings. In Fig. 6(b), after 192 hours of immersion, all the samples exhibited at less than two capacitive loops except for the steel substrate, which exhibited only one. In the case of the TiAlN matrix coating, the appearance of the loop at low frequencies (LF) could be related to the formation of a passive layer, and  $\text{TiO}_2$  or  $\text{Al}_2\text{O}_3$  oxides, during the electrochemical reaction with the electrolyte (Ref 58). In the Ag-doped coatings, the appearance of a new capacitive loop is related to the formation of a passive layer and the dissolution processes of the Ag nanoparticles. Similar impedance behavior was observed for all the samples at large immersion time, as shown in Fig. 6(c).

It is interesting to note the higher impedance exhibited by the TiAlN(Ag)-0.8at% coating for long exposure times when compared to the TiAlN matrix and the rest of the Ag-doped coatings. These results seem to correlate with the dense glass-like ceramic nature observed in the cross-section of this coating (Fig. 2b), in which the columnar grain limits are not appreciated, conversely to those observed for the rest of the coatings where the grain limits are evident. Presumably, during TiAlN(Ag)-0.8at% coating deposition, Ag particles tend to block the columnar structure growth, refining the microstructure and reducing the porosity of the coatings. This effect limits the filtration of the electrolyte into the coating and prevents it reaches the metallic substrate. Although the resistance of this coating decreased in one order of magnitude during the immersion for 192 hrs., as a consequence of silver dissolution, the TiAlN(Ag)-0.8at% coating exhibited the largest impedance of all the tested coatings. The exceptional performance of the TiAlN(Ag)-0.8at% coating was preserved until the end of the immersion test (360 hrs. of exposure time).

To explain more in detail the behavior of the coatings and the steel substrate at different immersion times in the corrosive medium, a fit of the experimental electrochemical impedance curves was made using equivalent electrical circuits (EEC). The EEC used to fit the EIS measurements for all samples is shown in Fig. 7. The parallel elements, resistors, and capacitors are introduced in the EECs because the total current through the working interface (interface between the working electrode and the electrolyte) is the sum of distinct contributions from the faradaic process,  $i_f$ , and double-layer charging,  $i_c$ . The double-layer capacitance is nearly a pure capacitance; hence it is represented in the equivalent circuit by the element  $Q_{dl}$ . In addition, the electrochemical impedance behavior of a coating or a passive layer can also be represented by a parallel combination of coating capacitance and resistance. Similar EEC models used to fit the electrochemical impedance response of a coated metal immersed in an electrolyte are usually found in literature reports (Ref 59-61).

For the AISI H11 steel substrate, the EEC is constituted by two-time constants, which obey to two capacitive loops (Fig. 7a). The capacitive loop at high frequencies (HF) represents the charge transference resistance ( $R_{ct}$ ) in parallel combination with the double layer capacitance ( $Q_{dl}$ ) in the oxide layer-steel interface. The capacitive loop at low frequencies (LF) corresponds to the parallel combination of resistance

and dielectric behavior of the passive layer formed on the surface of the steel ( $R_{oxide \text{ layer}}$  and  $Q_{oxide \text{ layer}}$ ).

The TiAlN coating matrix exhibited three capacitive loops in the electrochemical impedance results. The capacitive loop at high frequencies (HF) is related to a passive layer formed on the steel once the electrolyte reaches the metallic interface through the pores of the coating ( $R_{oxide \text{ layer}}$  and  $Q_{oxide \text{ layer}}$ ). The second capacitive loop at intermediate frequencies (MF) is related to the charge transfer resistance in a parallel combination with the double-layer capacitance of the metallic substrate ( $R_{ct}$  and  $Q_{dl}$ ), and the third capacitive loop at low frequencies (LF) is due to the resistive of the TiAlN coating ( $R_{coat \text{ layer}}$  and  $Q_{coat}$ ), as shown in Fig. 7(b). Finally, in the TiAlN(Ag) coatings and due to the presence of Ag nanoparticles in the top surface of the coatings, the capacitive loop at high frequencies (HF) is related to the charge transfer resistance ( $R_{Ag}$ ) in parallel combination with the double-layer capacitance of the Ag nanoparticles ( $Q_{Ag}$ ), see Fig. 7(c). The other two capacitive loops at intermediate and low frequencies are described similar to that of the TiAlN coating mentioned above but with the addition of a time constant, corresponding to the diffusion of the  $\text{Ag}^+$  ions toward the electrolyte in a finite diffusion layer (Porous Bounded Warburg Element-W), which is coupled to the LF loop.

The fitting parameter values of the experimental EIS measurements using electrical equivalent circuits after 15 days of sample immersion (end of the immersion test) are summarized in Table 4. It can be seen that the resistance of the Ag ( $R_{Ag}$ ) is the lowest value compared to the coat and charge transfer resistances,  $R_{coat}$  and  $R_{ct}$ , respectively. This is an expected result because in this kind of coatings silver dissolution and release of  $\text{Ag}^+$  ions to the electrolyte happen in chloride media and simulated body fluids (Ref 17, 57). Additionally, at the end of the immersion test, the TiAlN(Ag)-0.8at% sample exhibited the highest values of coating and charge transfer resistances ( $R_{coat}$  and  $R_{ct}$ ), which is in agreement with the highest corrosion protection property of this coating commented in the analysis of Fig. 5. The Q parameter of the TiAlN matrix coating showed the highest value after 15 days of immersion, probably associated with a semiconductor behavior of this coating, as reported by Akao et al. (Ref 62).

The evolution of the  $R_{coat}$ ,  $R_{Ag}$ , and  $R_{ct}$  with the time of the immersion of different samples is shown in Fig. 8. The results are in line with those obtained in previous works, indicating that the densification grade of coatings affects strongly the electrochemical activity (Ref 17, 57). In all the cases, the resistances exhibited by the TiAlN and Ag-doped TiAlN coatings were higher than those shown by the bare substrate during the whole immersion time (Fig. 8a). For this case, the values of the resistances presented by the coatings are very close to each other in time; however, even though the TiAlN coating matrix from the first hours showed the major value of resistance, at the end of the test, the TiAlN(Ag)-0.8at% coating exhibited the highest resistance respect to the other Ag-doped samples. As aforementioned, TiAlN(Ag)-0.8at% was the coating that exhibited the highest crystallinity, according to the XRD results, and according to the SEM observations, a glassy and fine microstructure. The high densification of TiAlN(Ag)-0.8at% coating induces the presence of low-grade grain limits hindering the contact of the electrolyte with the substrate. Regarding the resistance presented by silver as a doping element in the TiAlN coatings, it declines as the quantity of this

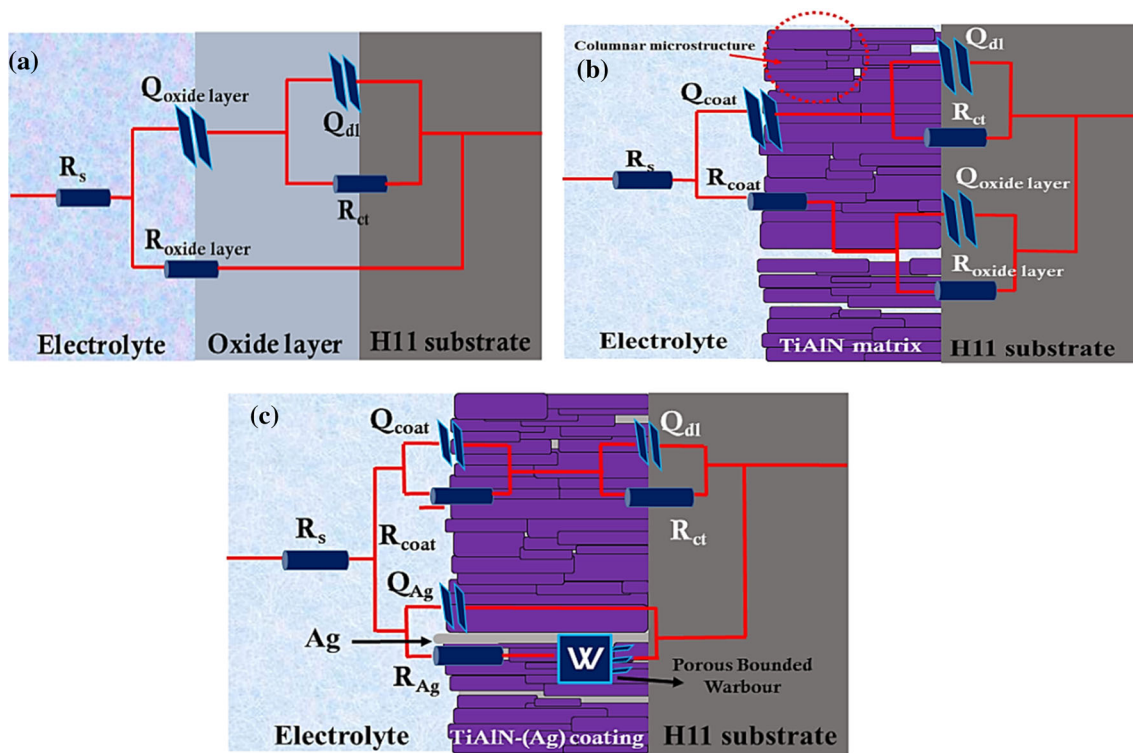


**Fig. 7** Electrical equivalent circuits used to fit the experimental EIS measurements of the samples. (a) H11 steel, (b) TiAlN matrix coating, and (c) TiAlN(Ag)-doped coatings

**Table 4** Values obtained by the fit of EIS measurements after 15 days of immersion, using the electrical equivalent circuits shown in Fig. 7

Sample	$R_{\text{oxide layer}} \Omega \text{ cm}^2$	$Q_{\text{oxide layer}} \mu\text{F cm}^{-2}$	$R_{\text{coat}} \Omega \text{ cm}^2$	$Q_{\text{coat}} \mu\text{F cm}^{-2}$	$R_{\text{Ag}} \Omega \text{ cm}^2$	$Q_{\text{Ag}} \mu\text{F cm}^{-2}$	$R_{\text{ct}} \Omega \text{ cm}^2$	$Q_{\text{dl}} \mu\text{F cm}^{-2}$	$W, \Omega^{-1} \text{ s}^{0.5}$
H11	29.26	2.22E-02	–	–	–	–	1.06E+03	1.38E-04	–
TiAlN	429.06	5.26E-04	202.16	3.43E-03	–	–	9.47E+03	6.14E-05	–
TiAlN(Ag)-0.8 at.%	...	...	325.32	3.41E-04	13.30	2.27E-04	1.25E+03	3.13E-03	1.57E-07
TiAlN(Ag)-10 at.%	...	...	173.30	8.42E-05	5.72	9.19E-04	6.92E+03	3.84E-03	9.29E-06
TiAlN(Ag)-20 at.%	...	...	158.67	2.95E-04	7.25	2.47E-03	5.60E+03	3.27E-03	3.37E-04
TiAlN(Ag)-25 at.%	...	...	77.14	4.45E-04	3.46	1.01E-02	2.68E+03	7.46E-03	1.31E-02

element increases in the coating, see Fig. 8(b). This result indicates that the electrochemical activity of silver in this type of system increases as the amount and size of Ag nanoparticles in the coating increase (Ref 17). This result can be associated with a greater dissolution tendency of the Ag particles than the TiAlN matrix, due to a nobler character of the matrix when compared to Ag, as seen further, in the polarization results. This means that in the TiAlN(Ag) coatings the TiAlN matrix preserves its high corrosion resistance character; meanwhile, the Ag nanoparticles are prone to dissolution. The dependence of Ag content into the coating on the silver dissolution has been reported by other authors (Ref 16, 63, 64). The TiAlN(Ag)-0.8at% sample exhibited the highest values of charge transfer resistance ( $R_{\text{ct}}$ ), practically during the whole immersion test,

see Fig. 8(c). A high value of  $R_{\text{ct}}$  is commonly related to low electrochemical activity and high corrosion resistance of the material. Consequently, better anticorrosion performance is expected for this coating than for the others.

**3.2.2 Potentiodynamic Polarization (PP).** Potentiodynamic polarization curves of the AISI H11 steel substrate, TiAlN matrix coating, and different TiAlN-Ag-doped coatings recorded at the end of the immersion test (15 days) are shown in Fig. 9. The most important corrosion parameters were extracted from the polarization curves by the Tafel extrapolation method, and they are summarized in Table 5.

It can be seen that the corrosion current density ( $i_{\text{corr}}$ ) of the TiAlN matrix coating was the lowest after 15 days of immersion, followed by the TiAlN(Ag)-0.8 at.% coating. This

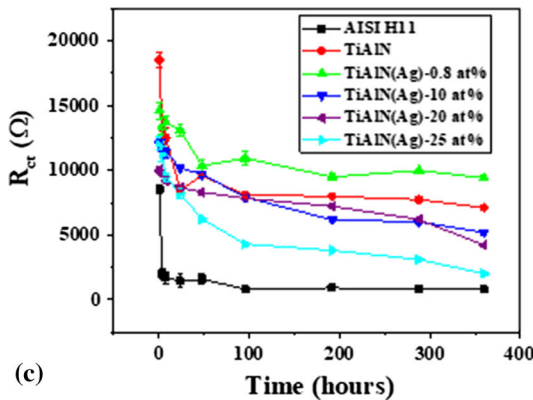
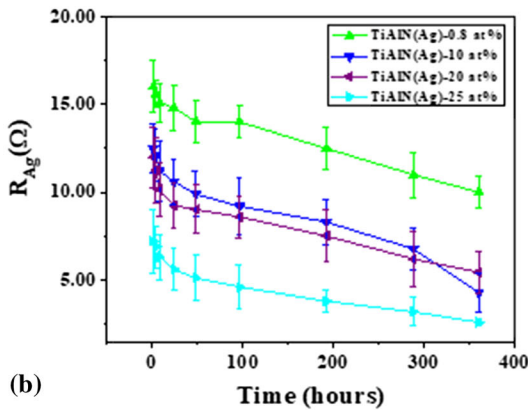
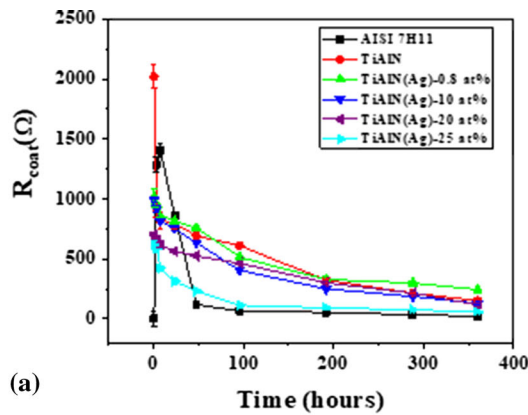


**Fig. 8** Resistance vs. time of immersion for the TiAlN(Ag) coatings, the TiAlN matrix, and the AISI H11 steel substrate in NaCl 3.5 wt.% electrolyte, at different exposure times, (a)  $R_{\text{coats}}$  ( $R_{\text{oxide}}$  for AISI H11), (b)  $R_{\text{Ag}}$ , and (c)  $R_{\text{ct}}$

would seem a contrary result to that observed in the impedance measurements, in which similar values of the impedance module were observed in the low-frequency limit (5mHz) in both TiAlN matrix and TiAlN(Ag)-0.8 at.% samples after 15 days of immersion. However, it should be taken into account that the Tafel extrapolation method for the determination of the corrosion current is a method that has limitations in coated samples since it is difficult to achieve a long linear region in the polarization curves in the near the corrosion potential. Therefore, the differences found in the corrosion current values in both coated samples are in the uncertainty of the experimental error.

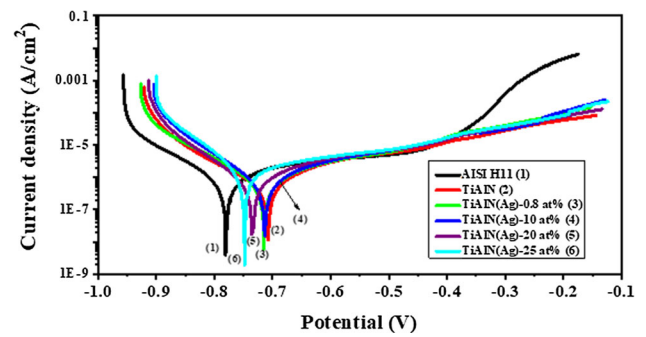


**Fig. 9** Potentiodynamic polarization curves of the AISI H11 steel, TiAlN and TiAlN(Ag) coatings with different contents of silver after 15 days of immersion in NaCl 3.5 wt.% solution

**Table 5** Corrosion parameters extracted from potentiodynamic polarization of H11 steel substrate, TiAlN matrix coating, and TiAlN-Ag-doped coatings in 3.5wt.% NaCl solution after 15 days of immersion

Sample	$i_{\text{corr}}$ $\mu\text{A}/\text{cm}^2$	$E_{\text{corr}}$ V	$b_c$ , V/dec	$b_a$ , V/dec
H11	0.75	-0.78	0.037	0.090
TiAlN	0.44	-0.70	0.102	0.248
TiAlN(Ag)-0.8 at.%	0.52	-0.71	0.073	0.230
TiAlN(Ag)-10 at.%	0.62	-0.71	0.079	0.242
TiAlN(Ag)-20 at.%	0.62	-0.73	0.075	0.254
TiAlN(Ag)-25 at.%	1.52	-0.75	0.054	0.278

In addition, corrosion potential ( $E_{\text{corr}}$ ) of the coated samples shifts to more positive potentials regarding the bare substrate, and cathodic ( $b_c$ ) and anodic ( $b_a$ ) Tafel slopes are larger than those exhibited by the substrate. These results mean that coatings based in TiAlN provide anticorrosive protection to the AISI H11 steel substrate in all the cases (Ref 65). Despite that the corrosion potential ( $E_{\text{corr}}$ ) of the coated samples shifts to more positive potentials respect to the bare substrate, the differences of the  $E_{\text{corr}}$  values, which are less than 80 mV, are not enough to induce galvanic corrosion, please see Fig 9 and Table 5. Furthermore, pitting or localized corrosion processes were not detected after electrochemical tests. The corrosion current density of the Ag-doped coating increased with the Ag content, resulting in agreement with the impedance results, which indicates an enhanced silver dissolution to the surrounding electrolyte as the Ag content into the coating systems increases. Although reductions in  $i_{\text{corr}}$  with respect to the substrate were observed in almost all Ag-doped coating, it is interesting to note that the TiAlN(Ag)-25 at.% coating showed the largest value of corrosion current density, even higher than that of the bare substrate. This fact can be correlated only with the enhanced silver dissolution from this coating. These results can be compared with the behavior against corrosion of similar systems previously investigated by our team, in which only the DC technique was used to obtain TiAlN (Ag, Cu) coatings (Ref 48). Conversely to that observed in DC-TiAlN (Ag, Cu) coatings, the hybrid technique HIPIMS-DC leads to more compact columnar grain structures, as a consequence better anticorrosion properties of the coatings can be achieved. TiAlN (Ag, Cu) coatings, manufactured from direct current, exhibited less dense structure and more negative corrosion potentials than

the substrate, in that case, it was AISI 420, indicating lower corrosion protection (Ref 48). In addition, it is worthy to mention that even at atomic percentages of dopant material (Ag, Cu) similar to those reported in the current work, the corrosion currents increased significantly. The degree of granular compaction offered by the hybrid HIPIMS-DC technique allowed to obtain corrosion potentials in all cases more positive than the substrate (H11 steel) and the corrosion current densities varied according to the degree of silver release.

## 4. Conclusions

TiAlN coatings with different Ag doping were deposited onto AISI H11 hot-working tool steel (HWS) using a hybrid DCMS/HiPIMS magnetron sputtering technique. The findings of this work contribute to fill a gap in the research area, particularly, in that concerning the development and study of the microstructure and electrochemical properties of Ag-doped TiAlN coatings deposited by hybrid DCMS/HiPIMS. Accordingly, the following conclusions are addressed:

1. The coatings showed defined surface columnar grain boundaries with a cauliflower-like microstructure which became rougher increasing the Ag-target power and Ag content into the TiAlN coatings. The ratio Ti:Al is almost 1:1 in the coatings, indicating that the face-centered cubic (fcc) structure is achieved, with which high mechanical and high wear resistance properties are expected. The presence of metallic Ag particles and Ag clusters into the coatings was confirmed by both DRX and XPS techniques.
2. The positive effect of the combination of HiPIMS and DC sputtering techniques is reflected in obtaining denser coatings than those normally obtained by DC sputtering alone, thanks to the high energetic deposition of HiPIMS. An almost dense glass-like structure with very fine columns was observed for the coating with 0.8 at% Ag. However, at higher silver contents, the columnar structure becomes more evident and the thickness of the columns increases, probably accompanied by an increase in the grain size and with a greater amount of silver lodged between the columns.
3. Through the study of the electrochemical response, it was confirmed that both the TiAlN matrix and the TiAlN(Ag) coatings showed higher impedance modules than that exhibited by the metallic substrate proving the corrosion protection conferred by the coatings. This was achieved because of the reduction in nanometric structural defects and cracks, conferred by Ag incorporation into the coatings, improving the protection of the metal substrate against corrosion by decreasing the number of direct electrolyte input channels to the substrate.
4. Taking into account that the values of the corrosion current of 0.44, 0.52, and 0.62 mA cm<sup>-2</sup> for the TiAlN and TiAlN doped with 0.8 and 10 at.%, respectively, do not present such a high difference, and that their corresponding potentials of corrosion of 0.70 and 0.71 V are also very similar, and that also the coating doped with 0.8 at.% has the highest corrosion resistance at long immersion times, it could be suggested that these two silver

doped coatings could be considered for applications where protection against and corrosion is required, for example, for extrusion and injection molds of polymeric materials.

## Acknowledgments

The authors are grateful to Departamento Administrativo de Ciencia, Tecnología e Innovación COLCIENCIAS for the financial support of this work (Contrat.768-2017). The authors also acknowledge the German Research Foundation (DFG) for supporting the development of the TiAlN hybrid coatings within the project Ti 343/34-2 and the German Academic Exchange Service (DAAD) in the scope of the project PPP-PROCOL 57394123.

## References

1. S.D. Jacobsen, R. Hinrichs, I.J.R. Baumvol, G. Castellano and M.A.Z. Vasconcellos, Depth Distribution of Martensite in Plasma Nitrided AISI H13 Steel and its Correlation to Hardness, *Surf. Coat. Technol.*, 2015, **270**, p 266–271. <https://doi.org/10.1016/j.surfcoat.2015.02.046>
2. G.B. Gaitan, M.G. Botero and M.A. Franco, Deposition and Characterization of Duplex Treated Coating System Applied on Hot Work Steel AISI H13, *Rev. Latinoam. Metal. y Mater.*, 2012, **32**, p 218–224
3. R.A. Mesquita, M. Kubin and R. Schneider, *Tool steels: Properties and performance*, CRC Press Taylor & Francis Group, New York, 2017
4. Y. Kayali, The Corrosion and Wear Behavior of TiN and TiAlN Coated AISI 316 L Stainless Steel, *Physicochem. Probl. Mater. Prot.*, 2014, **50**, p 412–419. <https://doi.org/10.1134/S207020511403006X>
5. V.M.C.A. De Oliveira, C. Aguiar, A.M. Vazquez, A.L.M. Robin and M.J.R. Barboza, Corrosion Behavior Analysis of Plasma-Assisted PVD Coated Ti-6Al-4V Alloy in 2 M NaOH Solution, *Mater. Res.*, 2017, **20**, p 436–444. <https://doi.org/10.1590/1980-5373-MR-2015-0737>
6. V.F.C. Sousa, F.J.G. Da Silva, G.F. Pinto, A. Baptista and R. Alexandre, Characteristics and Wear Mechanisms Of TiAlN-Based Coatings for Machining Applications: A Comprehensive Review, *Metals (Basel)*, 2021, **11**, p 1–49. <https://doi.org/10.3390/met11020260>
7. D.M. Mattox, *Handbook of physical vapor deposition ( PVD ) Processing, Film Formation, Adhesion, Surface, Preparation and contamination control*, Noyes Publications, U.S.A, New Jersey, 1998
8. K. Sarakinos, J. Alami and S. Konstantinidis, High Power Pulsed Magnetron Sputtering: A Review on Scientific and Engineering State of the Art, *Surf. Coat. Technol.*, 2010, **204**, p 1661–1684. <https://doi.org/10.1016/j.surfcoat.2009.11.013>
9. B. Gui, H. Zhou, J. Zheng, X. Liu, X. Feng and Y. Zhang, Microstructure and Properties of TiAlCrN Ceramic Coatings Deposited by Hybrid HiPIMS/DC Magnetron Co-Sputtering, *Ceram. Int.*, 2021. <https://doi.org/10.1016/j.ceramint.2020.11.175>
10. W. Tillmann, D. Grisales, D. Stangier, I. Ben Jebara, H. Hang, Influence of the Etching Processes on the Adhesion of TiAlN coatings Deposited by DCMS, HiPIMS and Hybrid Techniques on Heat Treated AISI H11. *Surf. Coat. Technol.*, 2019, **378**, p 125075
11. I. Ebrahimzadeh and F. Ashrafzadeh, The Influence of Temperature on the Frictional Behavior of Duplex-Coated Die Steel Rubbing Against Forging Brass, *J. Mater. Eng. Perform.*, 2014 <https://doi.org/10.1007/s11665-014-1301-4>
12. K.V. Chauhan and S.K. Rawal, A Review Paper on Tribological and Mechanical Properties of Ternary Nitride Based Coatings, *Procedia Technol.*, 2014, **14**, p 430–437. <https://doi.org/10.1016/j.protecy.2014.08.055>
13. J.M. Paiva, G. Fox-rabinovich, E.L. Junior, P. Stolf, Y. Seid, A. Id, M.M. Martins, C. Bork and S. Veldhuis, Tribological and Wear Performance of Nanocomposite PVD Hard Coatings Deposited on Aluminum Die Casting Tool, *Materials (Basel)*, 2018 <https://doi.org/10.3390/ma11030358>
14. D. Zheng, S. Zhu and F. Wang, The Influence of TiAlN and enamel Coatings on the Corrosion Behavior of Ti6Al4V Alloy in the Presence

- of Solid NaCl Deposit and Water Vapor at 450 °C, *Surf. Coat. Technol.*, 2007, **201**, p 5889–5864
15. M. Zhang, L. Xin, X. Ding, S. Zhu and F. Wang, Effects Ti/TiAlN Composite Multilayer Coatings on Corrosion Resistance of Titanium Alloy in Solid NaCl-H<sub>2</sub>O-02 at 600 °C, *J. Alloys Compd.*, 2018, **734**, p 307–317. <https://doi.org/10.1016/J.JALLCOM.2017.11.035>
  16. Q. Cai, S. Li, J. Pu, X. Bai, H. Wang, Z. Cai and X. Wang, Corrosion Resistance and Antifouling Activities of Silver-Doped CrN Coatings Deposited by Magnetron Sputtering, *Surf. Coat. Technol.*, 2018, **354**, p 194–202. <https://doi.org/10.1016/j.surfcoat.2018.09.006>
  17. A.M. Echavarría, J.A. Calderón and G. Gilberto Bejarano, Characterization of the Structure and Electrochemical Behavior of Ag-TaN Nanostructured Composite Coating for Biomedical Applications, *Surf. Coat. Technol.*, 2018 <https://doi.org/10.1016/j.surfcoat.2018.04.012>
  18. X. Liu, J. Kavanagh, A. Matthews and A. Leyland, The Combined Effects of Cu and Ag on the Nanostructure and Mechanical Properties of CrCuAgN PVD Coatings, *Surf. Coat. Technol.*, 2015, **284**, p 101–111. <https://doi.org/10.1016/J.SURFCOAT.2015.08.070>
  19. L. Incerti, A. Rota, S. Valeri, A. Miguel, J.A. García, R.J. Rodríguez and J. Osés, Nanostructured Self-Lubricating CrN-Ag Films Deposited by PVD arc Discharge and Magnetron Sputtering, *Vacuum.*, 2011, **85**, p 1108–1113. <https://doi.org/10.1016/j.vacuum.2011.01.022>
  20. A.M. Echavarría, S. Robledo and G. Gilberto Bejarano, Influence of Ag Nanoparticles on the Mechanical and Tribological Properties and on the Cytotoxic and Bactericidal Effects of TaN(Ag) Coatings, *Rev. Metal.*, 2017 <https://doi.org/10.3989/revmetalm.085>
  21. A.M. Echavarría and G. Bejarano G., J.M. Meza, Mechanical and Tribological Features of TaN(Ag-Cu) Duplex Nanocomposite Coatings: Their Response to Heat Treatment, *Ingeniare*, 2017 <https://doi.org/10.4067/S0718-33052017000400662>
  22. C. Dang, J. Li, Y. Wang, Y. Yang, Y. Wang and J. Chen, Influence of Ag Contents on Structure and Tribological Properties of TiSiN-Ag Nanocomposite Coatings on Ti–6Al–4V, *Appl. Surf. Sci.*, 2017, **394**, p 613–624. <https://doi.org/10.1016/j.apsusc.2016.10.126>
  23. H. Ju, L. Yu, D. Yu, I. Asempah and J. Xu, Microstructure, Mechanical and Tribological Properties of TiN-Ag Films Deposited by Reactive Magnetron Sputtering, *Vacuum*, 2017, **141**, p 82–88. <https://doi.org/10.1016/j.vacuum.2017.03.026>
  24. L. Yu, H. Zhao and J. Xu, Influence of Silver Content on Structure, Mechanical and Tribological Properties of WCN–Ag Films, *Mater. Charact.*, 2016, **114**, p 136–145. <https://doi.org/10.1016/j.matchar.2016.02.013>
  25. H.D. Mejía, A.M. Echavarría and G. Bejarano G., Influence of Ag-Cu Nanoparticles on the Microstructural and Bactericidal Properties of TiAlN(Ag, Cu) Coatings for Medical Applications Deposited by Direct Current (DC) Magnetron Sputtering, *Thin Solid Films*, 2019, **687**, p 137460. <https://doi.org/10.1016/j.tsf.2019.137460>
  26. H.D. Mejía V, D. Perea, G. Bejarano G, Development and Characterization of TiAlN(Ag,Cu) Nanocomposite Coatings Deposited by DC Magnetron Sputtering for Tribological Applications. *Surf. Coat. Technol.* 2020, **381**, p 125095
  27. F. Karabudak, R. Yeşildal, E.E. Şüküroğlu, S. Şüküroğlu, H. Zamanlou, N. Dikbaş, F. Bayındır, S. Şen and Y. Totik, An Investigation of Corrosion Resistance and Antibacterial Sensitivity Properties of Nano-Ag-Doped TiO<sub>2</sub> Coating and TiO<sub>2</sub> Coating Grown on NiTi Alloy with the Micro-Arc Oxidation Process, *Arab. J. Sci. Eng.*, 2017, **42**, p 2329–2339. <https://doi.org/10.1007/s13369-017-2463-9>
  28. E.E. Sukuroglu, Investigation of Antibacterial Susceptibility of Ag-Doped Oxide Coatings onto AZ91 Magnesium Alloy by Microarc Oxidation Method, *Adv. Mater. Sci. Eng.*, 2018, **2018**, p 6871241. <https://doi.org/10.1155/2018/6871241>
  29. G. Greczynski, L. Hultman and M. Odén, X-ray Photoelectron Spectroscopy Studies of Ti<sub>1-x</sub>Al<sub>x</sub>N (0 ≤ x ≤ 0.83) High-Temperature Oxidation: The Crucial Role of Al Concentration, *Surf. Coat. Technol.*, 2019, **374**, p 923–934. <https://doi.org/10.1016/j.surfcoat.2019.06.081>
  30. G. Greczynski, J. Jensen, J.E. Greene, I. Petrov and L. Hultman, X-ray Photoelectron Spectroscopy Analyses of the Electronic Structure of Polycrystalline Ti<sub>1-x</sub>Al<sub>x</sub>N Thin Films with 0 ≤ x ≤ 0.96, *Surf. Sci. Spectra.*, 2014, **21**, p 35–49. <https://doi.org/10.1116/11.20140506>
  31. G. Greczynski, J. Lu, M. Johansson, J. Jensen, I. Petrov, J.E. Greene and L. Hultman, Selection of Metal Ion Irradiation for Controlling Ti<sub>1-x</sub>Al<sub>x</sub>N Alloy Growth Via Hybrid HIPIMS/Magnetron Co-Sputtering, *Vacuum*, 2012, **86**, p 1036–1040. <https://doi.org/10.1016/j.vacuum.2011.10.027>
  32. G. Greczynski, J. Lu, J. Jensen, S. Bolz, W. Kölker, C. Schiffrers, O. Lemmer, J.E. Greene and L. Hultman, A Review of Metal-Ion-Flux-Controlled Growth of Metastable TiAlN by HIPIMS/DCMS co-Sputtering, *Surf. Coat. Technol.*, 2014, **257**, p 15–25. <https://doi.org/10.1016/j.surfcoat.2014.01.055>
  33. H. Chandler, V. Flint, R.L. Boring, C. Powers, Heat Treater's Guide Practices and Procedures for Irons and Steels, ASM Int. (1995)
  34. W. Tillmann, D. Grisales and D. Stangier, Effects of AISI H11 Surface Integrity on the Residual Stresses and Adhesion of TiAlN/Substrate Compounds, *Surf. Coat. Technol.*, 2019, **357**, p 466–472. <https://doi.org/10.1016/j.surfcoat.2018.10.032>
  35. M. Al Bukhaiti, K. Al-hatab, W. Tillmann, F. Hoffmann and T. Sprute, Tribological and Mechanical Properties of Ti/TiAlN/TiAlCN Nanoscale Multilayer PVD Coatings Deposited on AISI H11 Hot Work Tool Steel, *Appl. Surf. Sci.*, 2014, **318**, p 180–190
  36. C. Rebbholz, H. Ziegele, A. Leyland and A. Matthews, Structure, Mechanical and Tribological Properties of Nitrogen-Containing Chromium Coatings Prepared by Reactive Magnetron Sputtering, *Surf. Coat. Technol.*, 1999, **115**, p 222–229. [https://doi.org/10.1016/S0257-8972\(99\)00240-6](https://doi.org/10.1016/S0257-8972(99)00240-6)
  37. G.S. Kim, S.Y. Lee, J.H. Hahn, B.Y. Lee, J.G. Han, J.H. Lee and S.Y. Lee, Effects of the Thickness of Ti Buffer Layer on the Mechanical Properties of TiN Coatings, *Surf. Coat. Technol.*, 2003, **171**, p 83–90. [https://doi.org/10.1016/S0257-8972\(03\)00243-3](https://doi.org/10.1016/S0257-8972(03)00243-3)
  38. C. Huang, Deposition of (Ti, Al) N Films on A2 Tool Steel by Reactive r.f. Magnetron Sputtering, *Surf. Coat. Technol.*, 1995, **71**, p 259–266
  39. E. Uhlmann, B. Stawiszynski, C. Leyens, S. Heinze and F. Sammler, Hard Turning of Hot Work and Cold Work Steels with HiPIMS and DCMS TiAlN Coated Carbide Inserts, *CIRP Conf. High Perform. Cut.*, 2016, **46**, p 591–594. <https://doi.org/10.1016/j.procir.2016.03.231>
  40. W. Tillmann, D. Grisales, D. Stangier, I. Ben Jebara and H. Kang, Influence of the Etching Processes on the Adhesion of TiAlN Coatings Deposited by DCMS, HiPIMS and Hybrid Techniques on Heat Treated AISI H11, *Surf. Coat. Technol.*, 2019, **378**, p 1–15
  41. H.D. Mejía V, D. Perea and G. Gilberto Bejarano, Development and Characterization of TiAlN(Ag, Cu) Nanocomposite Coatings Deposited by DC Magnetron Sputtering for Tribological Applications. *Surf. Coat. Technol.*, 2020, **381**, p 125095. <https://doi.org/10.1016/j.surfcoat.2019.125095>
  42. P.A. Papi, C.P. Mulligan and D. Gall, CrN–Ag Nanocomposite Coatings: Control of Lubricant Transport by Diffusion Barriers, *Thin Solid Films*, 2012, **524**, p 211–217. <https://doi.org/10.1016/j.tsf.2012.10.010>
  43. S. Calderon Velasco, A. Cavaleiro and S. Carvalho, Functional Properties of Ceramic-Ag Nanocomposite Coatings Produced by Magnetron Sputtering, *Prog. Mater. Sci.*, 2016 <https://doi.org/10.1016/j.pmatsci.2016.09.005>
  44. Y.N. Kok and P.E. Hovsepian, Resistance of Nanoscale Multilayer C/Cr Coatings Against Environmental Attack, *Surf. Coat. Technol.*, 2006, **201**, p 3596–3605. <https://doi.org/10.1016/j.surfcoat.2006.08.109>
  45. Y. Xin, C. Liu, K. Huo, G. Tang, X. Tian and P.K. Chu, Corrosion Behavior of ZrN/Zr Coated Biomedical AZ91 Magnesium Alloy, *Surf. Coat. Technol.*, 2009, **203**, p 2554–2557. <https://doi.org/10.1016/j.surfcoat.2009.02.074>
  46. S.H. Ahn, J.H. Yoo, J.G. Kim and J.G. Han, On the Corrosion Behavior of Multilayered WC-Ti<sub>1-x</sub>Al<sub>x</sub>N Coatings on AISI D2 Steel. *Surf. Coat. Technol.* 163–64 (n.d.) 611–619. <http://cat.inist.fr/?aMode=afficheN&cpsid=14464939> (accessed June 29, 2016)
  47. D.A. Delisle and J.E. Krzanowski, Surface Morphology and Texture of TiAlN/CrN Multilayer Coatings, *Thin Solid Films*, 2012, **524**, p 100–106. <https://doi.org/10.1016/J.TSF.2012.09.073>
  48. C.P. Mulligan and D. Gall, CrN–Ag Self-Lubricating Hard Coatings, *Surf. Coat. Technol.*, 2005, **200**, p 1495–1500. <https://doi.org/10.1016/j.surfcoat.2005.08.063>
  49. T. de los Arcos, P. Oelhafen, U. Aebi, A. Hefli, M. Düggelin, D. Mathys, R. Guggenheim, Preparation and Characterization of TiN–Ag Nanocomposite Films, *Vacuum*, 2002, **67**, p 463–470. [https://doi.org/10.1016/S0042-207X\(02\)00232-4](https://doi.org/10.1016/S0042-207X(02)00232-4)
  50. S. Kumar, S.R. Maity and L. Patnaik, Friction and Tribological Behavior of Bare Nitrided, TiAlN and AlCrN Coated MDC-K Hot Work Tool Steel, *Ceram. Int.*, 2020, **46**, p 17280–17294. <https://doi.org/10.1016/j.ceramint.2020.04.015>
  51. O. Comakli, Improved Structural, Mechanical, Corrosion and Tribocorrosion Properties of Ti45Nb Alloys by TiN, TiAlN Monolayers, and

- TiAlN/TiN Multilayer Ceramics Films, *Ceram. Int.*, 2021, **47**, p 4149–4156
52. P. Zeman, Structure and Properties of Hard and Superhard Zr – Cu – N Nanocomposite Coatings, *Mater. Sci. Eng. A.*, 2000, **289**, p 189–197. [https://doi.org/10.1016/S0921-5093\(00\)00917-5](https://doi.org/10.1016/S0921-5093(00)00917-5)
  53. D. Gall, S. Kodambaka, M.A. Wall, I. Petrov and J.E. Greene, Pathways of Atomistic Processes on TiN(001) and (111) Surfaces During Film Growth: An ab Initio Study, *J. Appl. Phys.*, 2003, **93**, p 9086–9094. <https://doi.org/10.1063/1.1567797>
  54. A. Obrosov, R. Gulyaev, M. Ratzke, A. Volinsky, S. Bolz, M. Naveed and S. Weiß, XPS and AFM Investigations of Ti-Al-N Coatings Fabricated Using DC Magnetron Sputtering at Various Nitrogen Flow Rates and Deposition Temperatures, *Metals (Basel)*, 2017, **7**, p 52. <https://doi.org/10.3390/met7020052>
  55. R. Ananthakumar, B. Subramanian, A. Kobayashi and M. Jayachandran, Electrochemical Corrosion and Materials Properties of Reactively Sputtered TiN/TiAlN Multilayer Coatings, *Ceram. Int.*, 2012, **38**, p 477–485. <https://doi.org/10.1016/j.ceramint.2011.07.030>
  56. C.F. Almeida Alves, F. Oliveira, I. Carvalho, A.P. Piedade and S. Carvalho, Influence of Albumin on the Tribological Behavior of Ag – Ti (C, N) Thin Films for Orthopedic Implants, *Mater. Sci. Eng. C. Mater. Biol. Appl.*, 2014, **34**, p 22–28. <https://doi.org/10.1016/j.msec.2013.09.031>
  57. H.D. Mejía, A.M. Echavarría, J.A. Calderón and G. Gilberto Bejarano, Microstructural and Electrochemical Properties of TiAlN(Ag, Cu) Nanocomposite Coatings for Medical Applications Deposited by dc Magnetron Sputtering, *J. Alloys Compd.*, 2020, **828**, p 154396. <https://doi.org/10.1016/J.JALLCOM.2020.154396>
  58. L. Cunha, M. Andritschky, L. Rebouta and K. Pischow, Corrosion of CrN and TiAlN Coatings in Chloride-Containing Atmospheres, *Surf. Coat. Technol.*, 1999, **116–119**, p 1152–1160. [https://doi.org/10.1016/S0257-8972\(99\)00270-4](https://doi.org/10.1016/S0257-8972(99)00270-4)
  59. A. Amirudin and D. Thiény, Application of Electrochemical Impedance Spectroscopy to Study the Degradation of Polymer-Coated Metals, *Prog. Org. Coat.*, 1995, **26**, p 1–28
  60. D. Quintero, O. Galvis, J.A. Calderón, J.G. Castaño and F. Echeverría, Effect of Electrochemical Parameters on the Formation of Anodic Films on Commercially Pure Titanium by Plasma Electrolytic Oxidation, *Surf. Coat. Technol.*, 2014, **258**, p 1223–1231. <https://doi.org/10.1016/j.surfcoat.2014.06.058>
  61. I.C.P. Margarit-Mattos, EIS and Organic Coatings Performance: Revisiting Some Key Points, *Electrochim. Acta.* 2020, **354**, p 136725
  62. S.N. Akao, M.N. Umata, T.O. Hmi, Thin and Low-Resistivity Tantalum Nitride Diffusion Barrier and Giant-Grain Copper Interconnects for Advanced ULSI Metallization, *Jpn. J. Appl. Phys.*, 1999, **2401** p 4–9
  63. A. Mazare, A. Anghel, C. Surdu-Bob, G. Totea, I. Demetrescu and D. Ionita, Silver Doped Diamond-Like Carbon Antibacterial and Corrosion Resistance Coatings on Titanium, *Thin Solid Films*, 2018, **657**, p 16–23. <https://doi.org/10.1016/j.tsf.2018.04.036>
  64. T. Yetim, Corrosion Behavior of Ag-doped TiO2 Coatings on Commercially Pure Titanium in Simulated Body Fluid Solution, *J. Bionic Eng.*, 2016, **13**, p 397–405. [https://doi.org/10.1016/S1672-6529\(16\)60311-6](https://doi.org/10.1016/S1672-6529(16)60311-6)
  65. T. Wang and Z. J. L. Yan, F. Gao and G. Zhang, Self-Lubricating TiN/MoN and TiAlN/MoN Nano-Multilayer Coatings for Drilling of Austenitic Stainless Steel, *Ceram. Int.*, 2019, **45**, p 24248–24253. <https://doi.org/10.1016/j.ceramint.2019.08.136>

**Publisher's Note** Springer Nature remains neutral with regard to jurisdictional claims in published maps and institutional affiliations.